IEEE Access
Multidisciplinary | Rapid Review | Open Access Journal

Received July 3, 2020, accepted July 20, 2020, date of publication July 27, 2020, date of current version August 7, 2020.

Digital Object Identifier 10.1109/ACCESS.2020.3012160

A Novel Framework for Improving Pulse-Coupled Neural Networks With Fuzzy Connectedness for Medical Image Segmentation

PEIRUI BAI[1], (Member, IEEE), KAI YANG[1], XIAOLIN MIN[1], ZIYANG GUO[1], CHANG LI[1], YINGXIA FU[2], CHAO HAN[1], XIANG LU[1], AND QINGYI LIU[1], (Member, IEEE)

[1]College of Electronic Information Engineering, Shandong University of Science and Technology, Qingdao 266590, China
[2]College of Mining and Safety Engineering, Shandong University of Science and Technology, Qingdao 266590, China

Corresponding author: Qingyi Liu (lqy_raphael@163.com)

This work was supported in part by the National Natural Science Foundation of China under Grant 61471225.

ABSTRACT A pulse-coupled neural network (PCNN) is a promising image segmentation approach that requires no training. However, it is challenging to successfully apply a PCNN to medical image segmentation due to common but difficult scenarios such as irregular object shapes, blurred boundaries, and intensity inhomogeneity. To improve this situation, a novel framework incorporating fuzzy connectedness (*FC*) is proposed. First, a comparative study of the traditional PCNN models is carried out to analyze the framework and firing mechanism. Then, the characteristic matrix of fuzzy connectedness (*CMFC*) is presented for the first time. The *CMFC* can provide more intensity information and spatial relationships at the pixel level, which is helpful for producing a more reasonable firing mechanism in the PCNN models. Third, by integrating the *CMFC* into the PCNN framework models, a construction scheme of FC-PCNN models is designed. To illustrate this concept, a general solution that can be applied to different PCNN models is developed. Next, the segmentation performances of the proposed FC-PCNN models are evaluated by comparison with the traditional PCNN models, the traditional segmentation methods, and deep learning methods. The test images include synthetic and real medical images from the Internet and three public medical image datasets. The quantitative and visual comparative analysis demonstrates that the proposed FC-PCNN models outperform the traditional PCNN models and the traditional segmentation methods and achieve competitive performance to the deep learning methods. In addition, the proposed FC-PCNN models have favorable capability to eliminate inference from surrounding artifacts.

INDEX TERMS Medical image segmentation, pulse-coupled neural network, fuzzy connectedness, characteristic matrix.

I. INTRODUCTION

Medical image segmentation aims to delineate substructure or organ boundaries and assign each original pixel or voxel to a specific class [1]. Currently, it has important clinical applications, such as image-guided treatment, surgical planning, localization of the human body, organ labeling and lesion recognition [2], [3]. Abundant approaches for medical image segmentation are being proposed in the literature [4]. However, it is still a challenging problem due to the following factors. First, anatomical structures of the human body are complex and variable. It is hard to deal with similar intensities between objects and the background or statistical variability in biological tissue [5]. Second, medical image segmentation is a specified problem that heavily depends on idiosyncrasies of imaging modalities, *e.g.*, ultrasound, MRI, PET-CT images [6], or segmenting targets, *e.g.*, the chest and blood vessels [7]. Third, various medical data dimensions require efficient algorithms and strong computational capabilities [8].

In terms of the new trend in recent years, we divide medical image segmentation methods into five categories: region-based methods, edge-based methods, model-based methods, artificial neural networks and deep learning methods. Region-based methods assign pixels to a region according to intensity similarity or region homogeneity. The most

The associate editor coordinating the review of this manuscript and approving it for publication was Easter Selvan Suviseshamuthu.

popular region-based method is the thresholding approach, which focuses on how to obtain appropriate threshold values based on the statistical information of an image (*e.g.*, gray-level histogram or minimum cross-entropy) [9]. The region growing, watershed algorithm, fuzzy connectedness and graph-based approaches are important variants of thresholding that have been applied widely in medical image segmentation [10]. Moreover, typical unsupervised machine learning methods, such as k-means clustering, mean shift clustering, expectation maximization, are considered a branch of the region-based method [11]. The atlas-guided method is a powerful tool for medical image segmentation. It aims to find a one-to-one transformation that maps a presegmented atlas image to the target image. However, the atlas-guided method has difficulty when dealing with multiple substructures with complex backgrounds or moving objects [12]. Edge-based methods obtain object boundaries according to the changes in image appearance [13]. Parallel differential operators or serial detecting operators, the Canny edge detector [14], and Live-wire [15] are typical edge-based methods that have been extensively used in medical image segmentation. In addition, more efforts have been made to develop hybrid methods by combining a region-based method with an edge-based method to mitigate the deficiencies of the individual approaches [16]. Model-based methods, such as active shape models (ASMs) [17] or active appearance models (APMs) [18], are attractive branches in the computer vision and image analysis community. The deformable model is also an effective model-based technique for extracting anatomical structures, which has the capability to accommodate the variability in biological structures over time and across individuals [19]. Parametric deformable models (*e.g.*, snake [20]) and geometric deformable models (*e.g.*, level set [21], [22]) are traditional active contour models that have been widely used in medical image segmentation [23]. In addition, artificial neural networks (ANNs) are an important tool in medical image segmentation [24]. Various ANN models are employed to classify pixels or gray levels directly [25] and optimize the engine parameters for nodules [26]. In this method, a training procedure is necessary to determine the weights assigned to the connections between nodes of a massive parallel network. The trained ANN is then used to segment test data. Deep learning methods have recently been highlighted. Benefiting from their powerful identification and classification capabilities, deep learning methods have been introduced into medical image segmentation given a large volume of training data or labeling samples [27]. U-Net is a typical deep learning method that adopts a U-type structure and skip connection in the architecture [28],[29]. Subsequently, various variants of U-Net, such as U-Net-DL [30] and U-Net-GAN [31], have been proposed and applied.

Traditional artificial neural networks and deep learning methods are heavily dependent on the dataset and training procedure. By contrast, a pulse-coupled neural network is a single-layer, two-dimensional, laterally connected network that does not require training [32], [33]. Although PCNNs have been widely used in image processing fields such as image signature recognition, image segmentation and image enhancement, there are two main limitations when applying them in medical image segmentation [34]. First, the segmentation is easily affected by the external contours of false targets. This phenomenon is due to the firing mechanism of this method taking only intensity information into account. Second, the optimal values of the model parameters, such as controlling parameters and threshold values, are difficult to determine. In this paper, we propose to take advantage of the fuzzy connectedness (FC) strength, which is capable of overcoming the limitations of PCNNs. There are three main contributions in this work: 1) A systematic comparison and analysis of the representative PCNN models is carried out. 2) The FC-PCNN models are further developed by introducing the characteristic matrix of fuzzy connectedness (*CMFC*) into the PCNN framework. The results show that the *CMFC* can provide the spatial distance information of fuzzy objects, which is helpful for addressing complex medical images. 3) A general strategy of parameter tuning and seed point selection of the proposed FC-PCNN models is given as a demanded guide in practical applications.

The main contents of the paper are organized as follows. Section 2 briefly describes the traditional PCNN models and the FC algorithm. Section 3 presents details of the proposed FC-PCNN models. The experimental results and comparison analysis are shown in Section 4. The discussion and conclusion are given in Section 5 and Section 6, respectively.

II. RELATED WORK

A. THE PULSE-COUPLED NEURAL NETWORKS

The architecture of PCNN models is a two-dimensional connected lateral network with a single layer of integrate-and-fire neurons. Each neuron is considered a modified version of Eckhorn's cortical neuron [35].

The PCNN models consists of feeding input, linking input, modulating field and a pulse generator. The neuron receives signals from the feeding inputs and linking inputs. The feeding inputs receive signals from the neighboring pixels, while the linking inputs receive signals from the laterally connected neighboring neurons. Usually, the response of the linking inputs is faster. The synchronous stimulus and global coupled mechanism are essential features of PCNN models.

A standard discrete PCNN (Full-PCNN) can be expressed by the following iterative process [36]:

$$F_{i,j}[m] = e^{-\alpha_F} F_{i,j}[m-1] + V_F \sum_{k,l} \omega_{i,j,k,l} Y_{k,l}[m-1] + S_{i,j} \tag{1}$$

$$L_{i,j}[m] = e^{-\alpha_L} L_{i,j}[m-1] + V_L \sum_{k,l} \psi_{i,j,k,l} Y_{k,l}[m-1] \tag{2}$$

$$U_{i,j}[m] = F_{i,j}[m]\left(1 + \beta_1 L_{i,j}[m]\right) \tag{3}$$

$$Y_{i,j}[m] = \begin{cases} 1, & U_{i,j}[m] > T_{i,j}[m] \\ 0, & otherwise \end{cases} \tag{4}$$

$$T_{i,j}[m] = e^{-\alpha_T} T_{i,j}[m-1] + V_T Y_{i,j}[m] \tag{5}$$

where $F_{i,j}[m]$ represents the feedback input of the neuron in the (i,j) position and $L_{i,j}[m]$ is the linking term that represents the influence from the surrounding neurons. Only $F_{i,j}[m]$ receives the input stimulus $S_{i,j,}$ which represents the gray intensity of the image pixels in the (i,j) position. $U_{i,j}[m]$ is the internal activity of the neuron, and $T_{i,j}[m]$ is the dynamic threshold. $Y_{i,j}[m]$ represents the binary output of a neuron, which is determined by comparing the internal element with a monotonically decreasing dynamic threshold. V_F, V_L, and V_T denote the inherent potential of the feeding input, linking input and dynamic threshold, respectively. α_F, α_L, and α_T denote the decay rate of the feeding input, linking input and dynamic threshold, respectively. ω and ψ are the synaptic weight coefficients of the feeding and linking inputs, respectively. β_1 is a linking coefficient that reflects the linking strength between two neurons.

The advantages of PCNN models is that they do not require any training and have a simple architecture. However, appropriate selection of the model parameters is still a difficult problem at present [37]. One solution is to simplify the architecture of the Full-PCNN; examples of PCNNs with simplified Full-PCNN architectures are SPN [38], ICM [39], SCM [40], UL-PCNN [41], and SPCNN [42]. Alternatively, setting the parameters automatically is another direction [43]. Therefore, it might be a good choice to combine the two strategies [44]. Table 1 lists the formulae of five representative PCNNs. The Full-PCNN model has the most complicated architecture, which is expressed by five formulae and seven parameters. The linking part, also called the internal activity, is obtained by multiplying the linking input with the offset β and the feeding input. A comparison operation between the internal activity and a dynamic threshold value is used to determine whether the pixel is firing. An SPN, which is described by three formulae and four parameters, is one simplified model with adoption of a combined internal activity $U_{i,j}[m]$. $U_{i,j}[m]$ is updated by a constant-threshold strategy. The simplified architecture of SCMs and SPCNNs is very similar to that of SPNs. Their internal activity employs a dynamic threshold strategy. Similar to SPNs, SCM models also consist of three formulae and four parameters (γ is usually set to 1). When the sigmoid function of an SCM is replaced by a traditional firing condition, the SCM becomes an SPCNN, which is expressed by three formulae and three parameters. The ICM is the only model that retains the feeding input, pulse generator, and dynamic thresholding. It is described by three formulae and three parameters.

TABLE 1. Formulae, parameters and number of five representative PCNNs.

Model	Formulae	Parameters and Number
FULL-PCNN	$F_{i,j}[m] = e^{-\alpha_F}F_{i,j}[m-1] + \boldsymbol{V_F}\sum_{k,l}\omega_{i,j,k,l}Y_{k,l}[m-1] + S_{i,j}$ $L_{i,j}[m] = e^{-\alpha_L}L_{i,j}[m-1] + \boldsymbol{V_L}\sum_{k,l}\psi_{i,j,k,l}Y_{k,l}[m-1]$ $U_{i,j}[m] = F_{i,j}[m]\left(1+\boldsymbol{\beta_1}L_{i,j}[m]\right)$ $Y_{i,j}[m] = \begin{cases}1, & U_{i,j}[m] > T_{i,j}[m]\\ 0, & otherwise\end{cases}$ $T_{i,j}[m] = e^{-\alpha_T}T_{i,j}[m-1] + \boldsymbol{V_T}Y_{i,j}[m]$	Decay coefficients: α_F, α_L, and α_T Potential coefficients: V_F, V_L, and V_T Linking coefficient: β_1 7
SPN	$U_{i,j}[m] = U_{i,j}[m-1]e^{-\Delta m/\tau} + S_{i,j}[m] + \boldsymbol{V_U}\sum_{k,l}\rho_{i,j,k,l}Y_{k,l}[m-1]$ $Y_{i,j}[m] = \begin{cases}1, & if\ \boldsymbol{\gamma_1} < U_{i,j}[m]\\ 0, & otherwise\end{cases}$ $U_{i,j}[m] = \begin{cases}\boldsymbol{V_\gamma}, & if\ \gamma_1 < U_{i,j}[m]\\ 0, & otherwise\end{cases}$	Decay coefficient: τ Potential coefficients: V_U and V_γ Threshold coefficient: γ_1 4
ICM	$F_{i,j}[m] = \boldsymbol{f}F_{i,j}[m-1] + S_{i,j} + \rho_{i,j}\{Y[m-1]\}$ $Y_{i,j}[m] = \begin{cases}1, & if\ F_{i,j}[m] > \mathrm{T}_{i,j}[m-1]\\ 0, & otherwise\end{cases}$ $T_{i,j}[m] = \boldsymbol{g}T_{i,j}[m-1] + \boldsymbol{h}\mathrm{Y}_{i,j}[m]$	Feeding coefficient: f Threshold coefficients: g, h 3
SCM	$U_{i,j}[m] = \boldsymbol{f}U_{i,j}[m-1] + S_{i,j} + S_{i,j}\sum_{k,l}\rho_{i,j,k,l}Y_{k,l}[m-1]$ $Y_{i,j}[m] = \begin{cases}1, & 1/(1+\exp(-\boldsymbol{\gamma}(U_{i,j}[m]-\mathrm{T}_{i,j}[m]))\\ 0, & otherwise\end{cases}$ $T_{i,j}[m] = \boldsymbol{g}T_{i,j}[m-1] + \boldsymbol{h}Y_{i,j}[m]$	Feeding coefficient: f Threshold coefficients: g and h Output coefficient: γ 4
SPCNN	$U_{i,j}[m] = \boldsymbol{f}U_{i,j}[m-1] + S_{i,j} + S_{i,j}\sum_{k,l}\rho_{i,j,k,l}Y_{k,l}[m-1]$ $Y_{i,j}[m] = \begin{cases}1, & U_{i,j}[m] > T_{i,j}[m-1]\\ 0, & otherwise\end{cases}$ $T_{i,j}[m] = \boldsymbol{g}T_{i,j}[m-1] + \boldsymbol{h}Y_{i,j}[m]$	Feeding coefficient: f Threshold coefficients: g and h 3

B. FUZZY CONNECTEDNESS

Images produced by any imaging device are inherently fuzzy [45]. Fuzzy approaches are usually employed to handle the uncertainties and intensity gradations of digital images. Fuzzy connectedness (FC) is an important notion describing how image elements connect. It aims to address the geometric and topological variation directly on the given image and handle the uncertainties and intensity gradations in images as realistically as possible [46]. It is worth noting that the results of using fuzzy connectedness alone are easily disturbed by noise in medical images. In recent research, fuzzy connectedness has usually been integrated with other segmentation methods [47]. Both the local and global phenomena of imaging procedures are considered. That is, through a local fuzzy relation on image elements called *affinity* and a global fuzzy relation called *fuzzy connectedness*, the geometric and topological variations in a fuzzy object can be captured effectively. The *affinity* not only takes the spatial adjacency of every pair of *pixels* or *spels* (elements in 3-dimensional space) into account but also the similarity of the intensity values of the image elements.

The principle of FC is illustrated in Fig. 1. Assume that there are three object regions, namely, O_1, O_2, and O_3,

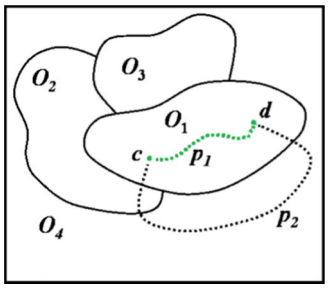

FIGURE 1. Illustration of the idea of underlying generalized fuzzy connectedness [46].

and a background O_4 in a gray-level image. Let c and d denote any two elements belonging to O_1, and let (c, d) denote a grid pair. P_1 and P_2 are two paths (a sequence of nearby elements) between elements c and d. Usually, there are two criteria to determine the strength of affinity. First, the closer the points are, the more adjacent the image elements are to each other. Second, the more similar the intensities of the image elements are, the greater the affinity between them. Therefore, the strength of a path is the smallest affinity of pairwise elements along the path. Contrary to the *affinity*, *fuzzy connectedness* tries to describe a global fuzzy relation between any two elements. Its strength is the strongest of all possible paths between pairwise elements. Taking the example of the affinity relation between elements c and d in O_1, it is expected that path P_1 has a higher strength than P_2, which traverses multiple object regions.

The critical notations of fuzzy connectedness in a fuzzy digital space (Z^n, ε) can be defined mathematically based on fuzzy subset theory. Here, Z^{n} represents an integer set that is a subset of n-dimensional Euclidean space R^{n}, c and d are two *spels* in Z^n, ε is the fuzzy *spel* adjacency. An example of fuzzy *spel* adjacency can be defined as follows [45]:

$$\mu_\omega(c,d) = \begin{cases} \dfrac{1}{1+\alpha\sqrt{\sum_{i=1}^{n}(c_i-d_i)^2}}, & if \ \sum_{i=1}^{n}|c_i-d_i| \le n \\ 0, & otherwise \end{cases} \tag{6}$$

where α is a nonnegative constant and n denotes the spatial dimension. The fuzzy *spel* adjacency is reflexive and symmetric, and it is desirable that it be a nonincreasing function. Let (C, f) represent a scene over (Z^n, ε) where C is called the scene domain ($c \in C$, $d \in C$), and f is a function whose domain is C. The fuzzy *spel* affinities can be expressed as follows:

$$\mu_k(c,d) = \frac{\mu_\omega(c,d)}{1+\beta_2|f(c)-f(d)|} \tag{7}$$

where β_2 is a nonnegative constant.

Let p_{cd} represent a nonempty path in (C, f) from *spel* c to d, *i.e.,* a sequence $< c(1), c(2), \ldots, c(\zeta) >$ *of* $\zeta \ge 2$ *spels*, P_{cd} represents the set of all paths from c to d including the empty and nonempty paths. Then, for all $p \in P_{(C,f)}$, a fuzzy subset called the fuzzy *k-net* N can be defined as follows:

$$\mu_N(p) = min[\mu_k\left(c^{(1)}, c^{(2)}\right), \mu_k\left(c^{(2)}, c^{(3)}\right), \ldots, \mu_k\left(c^{(\zeta-1)}, c^{(\zeta)}\right)] \tag{8a}$$

$$\mu_N(<>) = 0 \tag{8b}$$

The fuzzy k-connectedness K representing a fuzzy relation in (C, f) can be defined as follows:

$$\mu_K(c,d) = \max_{p \in P_{cd}}[\mu_N(p)] \tag{9}$$

For any $\theta \subset [0, 1]$ and $(c, d) \in C$, a binary relation K_θ in C can be defined as follows:

$$\mu_{K_\theta}(c,d) = \begin{cases} 1, & if \ \mu_K(c,d) \in \theta \\ 0, & otherwise \end{cases} \tag{10}$$

Finally, a fuzzy K_{θ_x}*-object* of (C, f) is a fuzzy k-component of strength θ_x, which can be defined by a membership function as follows:

$$\mu_{O_{\theta_x(o)}}(c) = \begin{cases} f(c), & if \ c \in [o]_{\theta_x} \\ 0, & otherwise \end{cases} \tag{11}$$

where $\theta_x = [x, 1]$ for $0 \le x \le 1$. $[o]_{\theta_x}$ denotes the equivalence class of K_{θ_x} that contains o for any $o \in C$. The process of finding the fuzzy K_{θ_x}*-object* can be considered an extraction of n-fuzzy objects problem. By applying a simple thresholding operation in the *Ko*-scene at an appropriate strength of connectedness, the extraction of the n-fuzzy object becomes naturally n-segmented to find the connecting *spels*.

III. THE PROPOSED FC-PCNN MODEL

PCNN models are attractive due to their simple architecture and lack of training requirements. However, they often fail when handling scenarios involving irregular objects or background clutter in medical image segmentation. Therefore, a novel and general strategy to complement the strength of PCNN models and FC is presented. By integrating prior knowledge of fuzzy objects into the PCNN model framework, the proposed FC-PCNN model can achieve robust and accurate segmentation.

First, a characteristic matrix of fuzzy connectedness (*CMFC*) providing spatial information of the adjacent pixels is computed. Let I represent a given digital image with L lines and J columns. The size or number of pixels is $D = L \times J$. Let i ($i \in L$) denote the line number and j ($j \in J$) denote the column number. Given a set S of the selected seed pixels, the fuzzy k-connectedness $\mu_K(\vartheta, s)$ is computed for every pixel. $\vartheta \in [1, D]$ denotes the index of the fuzzy k-connectedness. The total of fuzzy k-connectedness is D, which is equal to the image size. A strategy of searching for an optimal path is applied during the process of computing the FC matrix of image pixels relative to the seed points. Starting from the seed point s, the optimal path is determined by searching the neighborhood range step by step. s is constantly optimized and replaced in the iterative

procedure when traversing the image, and the largest FC value, which reflects the optimal path between non-seed point pixels and seed pixels, will be found. Then, the *CMFC* (the final FC matrix) will be obtained by configuring the fuzzy k-connectedness as follows:

$$CMFC_{\vartheta,s} = \begin{bmatrix} \mu_K(1,s) & \mu_K(L+1,s) & \mu_K(D-L,s) \\ \mu_K(i,s) & \cdots & \mu_K(D-L+1,s) \\ \vdots & \cdots & \vdots \\ \mu_K(L,s) & \mu_K(2\times L-1,s) & \mu_K(D,s) \end{bmatrix} \tag{12}$$

Second, the FC matrix $CMFC_{\vartheta,s}$ is employed to play the same role as $S_{i,j}$ in the original PCNN models. This operation is feasible due to the same dynamic range and size of $CMFC_{\vartheta,s}$ and $S_{i,j}$, whose values are both between 0 and 1. The primary advantage of $CMFC_{\vartheta,s}$ is that it optimizes the firing mechanism of the PCNN models. In the traditional PCNN models, the pixels with the greatest response at different places in the whole image are fired first. However, this mechanism may lead to pixels in the region of noise or false targets being fired. By adopting $CMFC_{\vartheta,s}$, the FC-PCNN models fire the pixels with the greatest response in the range limited by the FC matrix. Thus, the interference of noise or artifacts can be reduced effectively. The flow chart of the PCNN and the proposed FC-PCNN models is illustrated in Fig. 2. The calculation process of the PCNN models is shown in the dotted box on the left and that of the FC method is shown in the dotted box on the right. The bold solid line denotes the connecting relationship between the two blocks that reflect the procedure of inputting the FC matrix into the PCNN model. It should be noted that this is a general integrated solution.

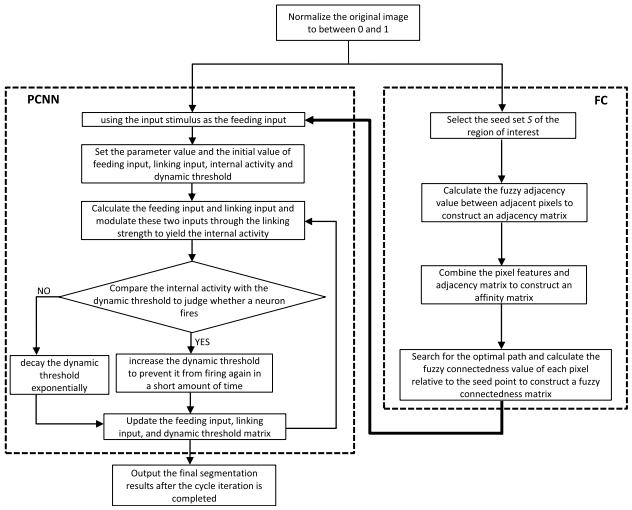

FIGURE 2. Flow chart of the PCNN and proposed FC-PCNN models.

IV. EXPERIMENTS AND RESULTS

Segmentation experiments on test images from the benchmark and medical images from three public datasets are used to evaluate the performance of the proposed FC-PCNN models. The Public Domain Database for Computational Anatomy (PCCDA) is provided by Harvard Medical School (http: //www.imagenglab.com/newsite/pddca/). It contains 48 labeled volumetric CT scans with a scan range from head to chest. The TCGA-LIHC dataset http://doi.org/10.7937/K9/TCIA.2016.IMMQW8UQ) is provided by The Cancer Genome Atlas (TCGA) and contains 125,397 images from 97 patients. The 3D-IRCADb-01 dataset (https://www.ircad.fr/research/3d-ircadb-01/) is composed of the 3D CT scans of 10 women and 10 men with hepatic tumors in 75% of cases. Segmentation experiments of 232 images from these three datasets and 16 single images were carried out in our study; only part of the segmentation results is shown in this section considering the space. All the experiments are implemented in MATLAB R2016a on a PC equipped with Intel Core i5-520 CPU 2.67 GHz and 8 GB RAM. The operating system is Windows 7 Service Pack 1.

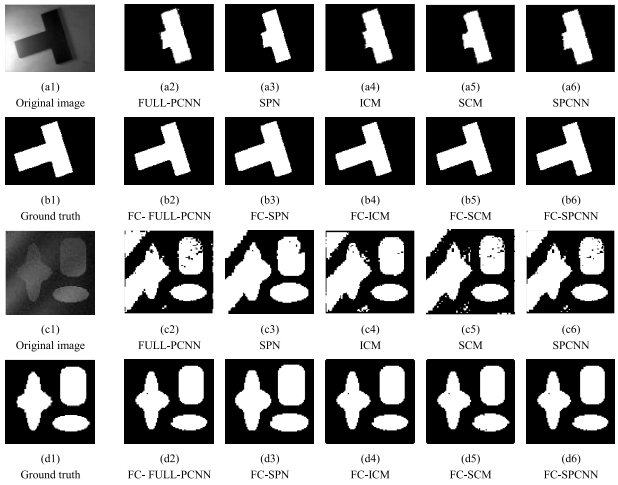

FIGURE 3. Comparison of the segmentation results from the five representative FC-PCNN models and the corresponding PCNN models. The two test images are synthetic images. (a1) T-shape.bmp. (c1) ThreeObj.bmp. (b1) and (d1) show the ground-truth images. (a2)-(a6) and (c2)-(c6) present segmentation results of the FULL-PCNN, SPN, ICM, SCM, SPCNN models, respectively. (b2)-(b6), and (d2)-(d6) present segmentation results of the corresponding FC-PCNN models, respectively.

A. COMPARISON WITH THE TRADITIONAL PCNN MODELS

To confirm that our framework is a general solution for different PCNN models, a comparison of five representative FC-PCNN models, *i.e.,* FC-Full-PCNN, FC-SPN, FC-ICM, FC-SCM, and FC-SPCNN with the corresponding traditional PCNN models are carried out in this section. Fig. 3 illustrates the segmentation results of two synthetic images. Evaluating the performance is easy since the target is known. Fig. 3(a1) and Fig. 3(c1) show the original images T-shape.bmp and ThreeObj.bmp, respectively. Fig. 3(b1) and Fig. 3(d1) show the manual segmentation results, which will be used as ground-truth images to compute quantitative indices.

The segmentation results of the FULL-PCNN, SPN, ICM, SCM, and SPCNN models are shown in the first and third rows from the 2nd column to the 6th column,

respectively (Figs. 3(a2)-(a6), Figs. 3(c2)-(c6)). The corresponding segmentation results of the FC-FULL-PCNN, FC-SPN, FC-ICM, FC-SCM, FC-SPCNN models are shown in the second and fourth rows from the 2nd column to the 6th column, respectively (Figs. 3(b2)-(b6), (d2)-(d6)). It can be clearly observed that the proposed FC-PCNN models outperform the corresponding PCNN models. The phenomena of incomplete target structure and serious pseudotargets can be observed in the segmentation results of all five traditional PCNN models to different degrees, whereas all the FC-PCNN models obtain satisfactory segmentation results by adopting the *CMFC*. As the spatial information of adjacent pixels is exploited, the proposed FC-PCNN models show better capability of target localization, noise reduction, and handling intensity inhomogeneity.

Fig. 4 illustrates the segmentation results of five real medical images, namely, Liver_A.jpg, Liver_B.png, Brain.bmp, Lung.png, and Kidney.png, with the five traditional PCNN models and the corresponding FC-PCNN models similarly. Liver_A.jpg and Brain.bmp are selected from the benchmark in the related studies. Brain.bmp is an MR image, and the other medical images are CT images. Live_B.png comes from the TCGA-LIHC dataset, Lung.png comes from the PCCDA dataset, and Kidney.png comes from the 3D-IRCADb-01 dataset. Figs. 4(a1), (c1), (e1), (g1), and (i1) show the original images. Figs. 4(b1), (d1), (f1), (h1), and (j1) illustrate the manual segmentation results. Figs. 4(a2)-(a6), (c2)-(c6), (e2)-(e6), (g2)-(g6), and (i2)-(i6) show the segmentation results of the FULL-PCNN, SPN, ICM, SCM, and SPCNN models, respectively. The segmentation results of the corresponding FC-PCNN models are shown in Figs. 4(b2)-(b6), (d2)-(d6), (f2)-(f6), (h2)-(h6), and (j2)-(j6).

Similar to Fig. 3, all five PCNN models obtain unacceptable results. They cannot ignore the influence of surrounding artifacts to obtain correct object contours, *e.g.*, the CT scanning bed in Fig. 4(g1) or the skull boundary in Fig. 4(c1). In contrast, the proposed FC-PCNN models achieve satisfactory results for all five test images. This finding indicates that only considering intensity information is not enough to extract targets from complex backgrounds. By providing spatial information of adjacent pixels as well as considering the fuzzy properties of the detected objects, the proposed FC-PCNN models are better at object localization and small target detection than the traditional models. As shown in Figs. 4(b2)-(b6), the FC-PCNN models detect the small vessel or biliary duct well, which are hard to identify manually. A quantitative comparison is also conducted. The Dice coefficient is a popular index that reflects how similar the segmented image is to the ground truth. However, the Dice coefficient has difficulty evaluating the segmentation performance if identifying the local error segmented region is difficult. Therefore, we adopt five quantitative indices: Dice coefficient, accuracy, precision, specificity, and sensitivity [43]. The formulae of the five metrics are as follows:

$$Dice = \frac{2TP}{(TP + FP) + (TP + FN)} \tag{13-1}$$

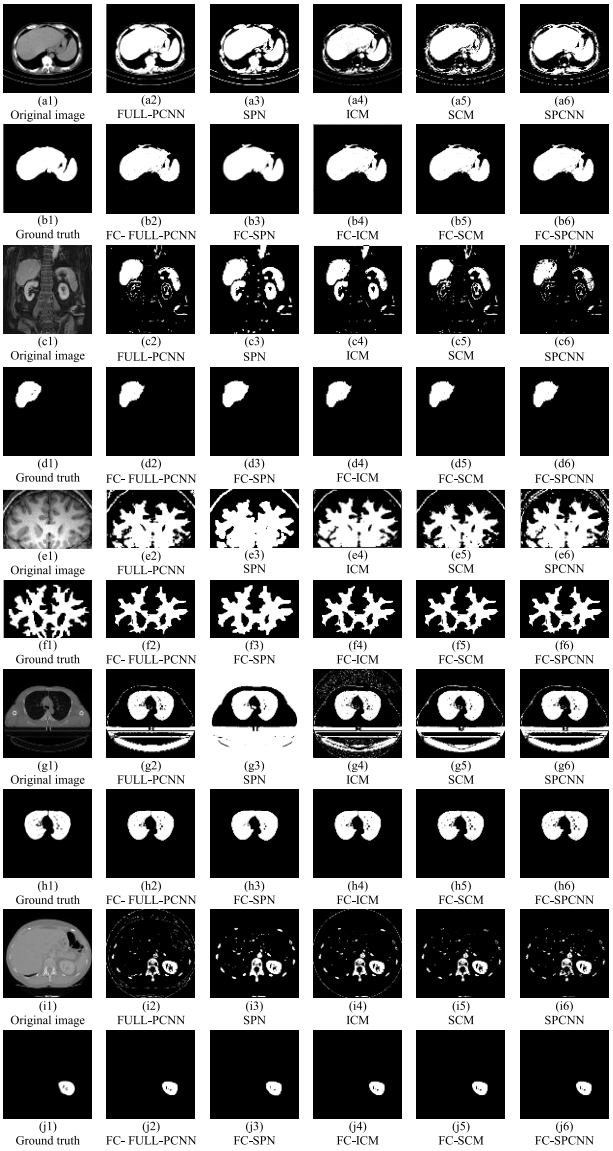

FIGURE 4. Comparison of the segmentation results between the five FC-PCNN models and the corresponding PCNN models using five medical images. (a1), (c1), (e1), (g1), and (i1) are the original images; (b1), (d1), (f1), (h1), and (j1) are the ground-truth images; (a2)-(a6), (c2)-(c6), (e2)-(e6), (g2)-(g6), and (i2)-(i6) are the segmentation results of the FULL-PCNN, SPN, ICM, SCM, and SPCNN models, respectively; (b2)-(b6), (d2)-(d6), (f2)-(f6), (h2)-(h6), and (j2)-(j6) segmentation results of the corresponding FC-PCNN models, respectively.

$$Accuracy = \frac{TP + TN}{TP + FP + TN + FN} \tag{13-2}$$

$$Precision = \frac{TP}{TP + FP} \tag{13-3}$$

$$Specificity = \frac{TN}{FP + TN} \tag{13-4}$$

$$Sensitivity = \frac{TP}{TP + FN} \tag{13-5}$$

where TP means the number of true positives (correctly segmented object pixels), FP means the number of false positives (incorrectly segmented object pixels), FN means the number of false negatives (incorrectly segmented nonobject pixels),

TABLE 2. Comparison of the Dice coefficients of the segmentation results of the PCNNs (Fig. 3 and Fig. 4).

Image	FULL-PCNN /FC-FULL-PCNN (Rate of increase)	SPN /FC-SPN (Rate of increase)	ICM /FC-ICM (Rate of increase)	SCM /FC-SCM (Rate of increase)	SPCNN /FC-SPCNN (Rate of increase)
T-shape	0.77/0.95 (23.4%)	0.73/0.98 (34.2%)	0.75/0.95 (26.7%)	0.74/0.95 (28.4%)	0.76/0.95 (25.0%)
ThreeObj	0.78/0.96 (23.1%)	0.78/0.94 (20.6%)	0.80/0.96 (20.0%)	0.77/0.96 (24.7%)	0.79/0.96 (21.5%)
Liver_A	0.77/0.96 (24.7/%)	0.76/0.97 (27.6%)	0.85/0.94 (10.6%)	0.80/0.96 (20.0%)	0.81/0.96 (18.5%)
Liver_B	0.66/0.95 (43.9%)	0.52/0.96 (84.6%)	0.52/0.95 (82.7%)	0.63/0.95 (50.8%)	0.68/0.95 (39.7%)
Brain	0.76/0.79 (3.9%)	0.75/0.86 (14.7%)	0.77/0.79 (2.6%)	0.77/0.79 (2.6%)	0.75/0.79 (5.3%)
Lung	0.63/0.98 (55.6%)	0.26/0.96 (269.2%)	0.63/0.98 (55.6%)	0.61/0.98 (60.7%)	0.62/0.98 (58.1%)
Kidney	0.41/0.95 (131.7%)	0.46/0.96 (108.7%)	0.45/0.95 (111.1%)	0.50/0.95 (90.0%)	0.52/0.95 (82.7%)

and *TN* means the number of true negatives (correctly segmented nonobject pixels).

Table 2 lists the Dice coefficients of the segmentation results in Fig. 3 and Fig. 4. The Dice coefficients obtained from the FC-PCNN models increase markedly in almost all the test images except for the Brain image. The relatively small increase for the Brain image (ranging from 2.6% to 14.7%) is due to the complex structure of cerebral white matter. However, the segmentation results are visually acceptable. The average Dice coefficient of the proposed FC-PCNN models is 0.96, which is 41.87% higher than that of the corresponding PCNN models. For further clarification, a statistical analysis over all the test images for this observation is conducted. Each P value from the Wilcoxon signed-rank tests for the five PCNN models vs the representative FC-FULL-PCNN model is 0.01563. This finding indicates that the proposed FC-PCNN models can significantly improve the segmentation accuracy ($p<0.05$).

Fig. 5 shows the other four indices of the segmentation results in Fig. 3 and Fig. 4 obtained by the FC-PCNN models. The performances of the five FC-PCNN models are stable for almost all the test images. Most values of the four indices are greater than 0.90. This finding indicates that the percentage of correct results with respect to all the results, the percentage of the accurately identified regions with respect to all regions, the percentage of the accurately identified regions with respect to all regions, and the capability of not detecting the unwanted regions are satisfactory. A larger index fluctuation for the Brain image implies that the quantitative indices may be unreliable when dealing with complex shapes. In this case, it is best to combine visual observation with quantitative analysis. In addition, the area under the curve (AUC) value of the segmentation results is also computed. The average values of the AUC for the five PCNN models and the corresponding FC-PCNN models are (0.8391, 0.8411, 0.8347, 0.8791, 0.8622) and (0.9513, 0.9794, 0.9324, 0.9398, 0.9330), respectively. These values mean that the pixel classification accuracy of the FC-PCNN models is higher than that of the PCNN models.

In addition, we compare the results considering the fuzzy connectedness alone and the proposed FC-PCNN method on seven test images. The first and second rows of Fig. 6 show the original images and manual segmentation results, respectively. The third and fourth rows present the segmentation results considering the FC alone and the FC-SPN, respectively. It can be observed that the FC-SPN performs better than the FC for almost all the test images. Only for the T-shaped image, which has clear and simple object contours, do both methods show similar performance.

B. COMPARISON WITH TRADITIONAL SEGMENTATION METHODS

With the above test images, we compare the FC-SPN model with five traditional segmentation methods whose principle is similar to that of PCNNs or FC to some degree. The five methods are the region growing, thresholding, local adaptive thresholding [48], mean shift [49], and fully connected conditional random field (FCCRF) [50] methods. Region growing and thresholding methods are traditional methods widely used in medical image segmentation. Local adaptive thresholding is a typical nonparametric method. Mean shift is an unsupervised clustering method. FCCRF is a probabilistic and nonparametric method. The parameters of each comparison method are tuned carefully to obtain satisfactory results.

Fig. 7 demonstrates the comparison results of the seven test images. The first and second columns show the original images and manual segmentation results, respectively. The segmentation results of the five traditional methods and the FC-SPN are illustrated in columns from the 3rd column to the 8th column. The FC-SPN obtains acceptable segmentation results for all the test images. The region growing method works well for four images, but it is ineffective for T-shape, ThreeObj, and Brain images. The local adaptive thresholding method is only valid for the T-shape image. All the other segmentations are inferior. Similar to the observations in Fig. 3 and Fig. 4, the traditional methods have difficulty reducing the interference of surrounding artifacts, heavy noise or severe intensity inhomogeneity. The FC-SPN not

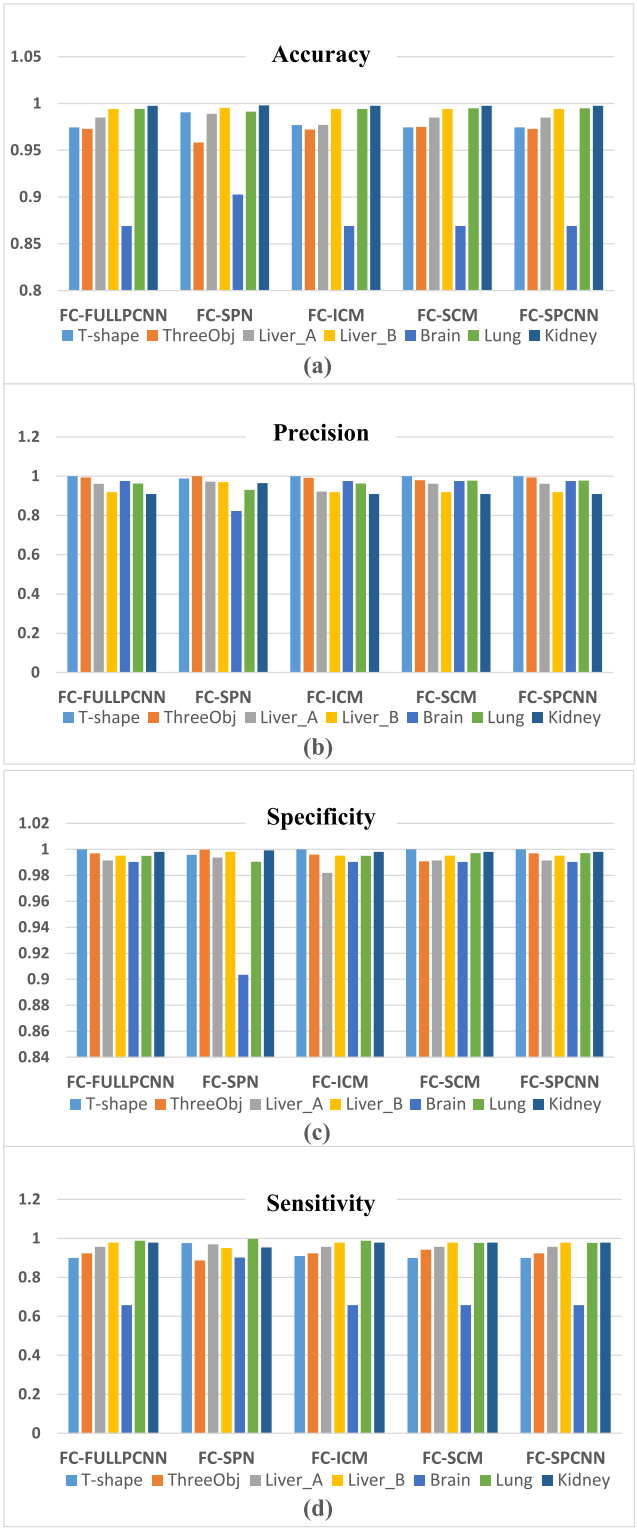

FIGURE 5. Four evaluation indices for the segmentation results in Fig. 3 and Fig. 4, which are obtained by using the FC-FULL-PCNN, FC-SPN, FC-ICM, FC-SCM, and FC-SPCNN models. (a) accuracy, (b) precision, (c) specificity, and (d) sensitivity.

only takes intensity information into consideration (global information) but also considers the spatial information and fuzzy property of adjacent pixels (local information), which

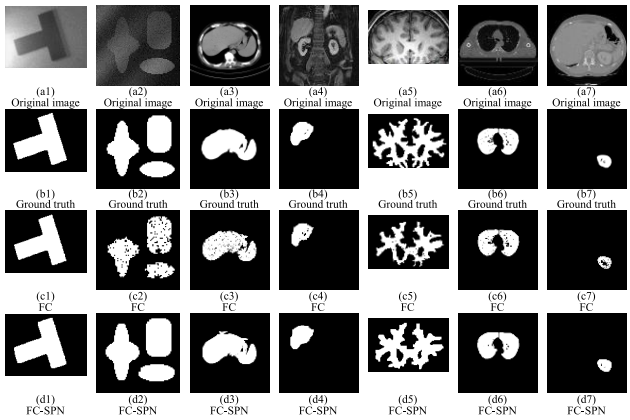

FIGURE 6. Segmentation results of the seven test images obtained from the FC and the FC-SPN methods. The first row to fourth row show the original image, ground truth, FC segmentation results and FC-SPN segmentation results, respectively.

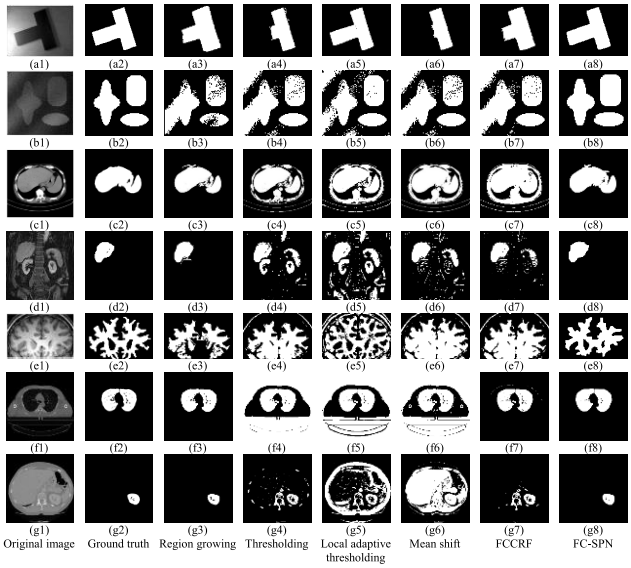

FIGURE 7. Segmentation results of the seven test images obtained from the five traditional segmentation methods and the FC-SPN model. The name of each method is marked at the bottom of the figure. The first and second columns show the original images and ground truth, respectively. In the 3rd column to the 8th column, the segmentation results of the six comparison methods are illustrated.

is why it outperforms the other methods. Although mean shift and local adaptive thresholding also consider local information, it seems that their robustness, generality, and accuracy cannot be guaranteed.

C. COMPARISON WITH DEEP LEARNING METHODS

Deep learning methods have been a hot topic in the field of artificial intelligence and computer vision since 2012 [51]. In recent years, it has been introduced into medical image segmentation as well. In this section, a comparison between deep learning methods and the proposed FC-PCNN model is carried out to further confirm the effectiveness and generality of the proposed model. Although deep learning method have different principles and mechanisms from those of the

FC-SPN model, it has no effect on the results and conclusion. Here, popular deep learning networks, FCN [52] and U-Net [28], [29], are chosen for comparison because of their powerful performance in medical image segmentation. The first step is preparing the training data. Here, the PCCDA dataset from the "Medical Image Computing and Computer Assisted Interventions (MICCAI) Challenge 2015" is employed. First, 10 randomly selected scan slices of pulmonary space from 16 randomly selected CT volumes are extracted. Then, the 160 lung CT slices are used as the training set of the FCN and U-Net. The other 24 pulmonary space slices extracted from two volumetric CT scan datasets (*i.e.*, C0017 and C0806) are used as the test set. The FCN transforms the fully connected layers in a traditional CNN into convolution layers one by one. First, multiple convolution and pooling operations are conducted to obtain the feature map. Then, 3 deconvolution operations are used to expand the pixels, and the final segmentation results are finally output. U-Net is a 9-layer deep network that adopts an encoder-decoder network and skip connections. The size of the input images and output images is 512 $\times$ 512 pixels. The training parameters, *e.g.*, steps per epoch and number of epochs, are set to 300 and 1, respectively.

Fig. 8 displays representative results. The first and second columns illustrate the original images and ground truth, respectively. The third to fifth columns present the segmentation results of the FCN, U-Net and FC-SPN models, respectively. It is obvious that the FCN, U-Net and FC-SPN models all capture the exact outline of the left and right lungs. The main difference occurs in small targets, such as pulmonary microvessels, which are hard to identify.

By visual inspection and quantitative comparison, the results of the FC-SPN model seem closest to the ground truth. The average values of the five indices for the FCN, U-Net and FC-SPN for the 11 CT images are (0.9907, 0.9808, 0.9978, 0.9295, 0.9542), (0.9933, 0.9890, 0.9988, 0.9463, 0.9671) and (0.9940, 0.9552, 0.9945, 0.9890, 0.9717), respectively. These findings imply that the FC-SPN, FCN and U-Net all perform well. However, the FCN and U-Net might not work well and might not be practical when training data are not easy to acquire. Therefore, the FC-SPN model is a good choice when there are few available samples.

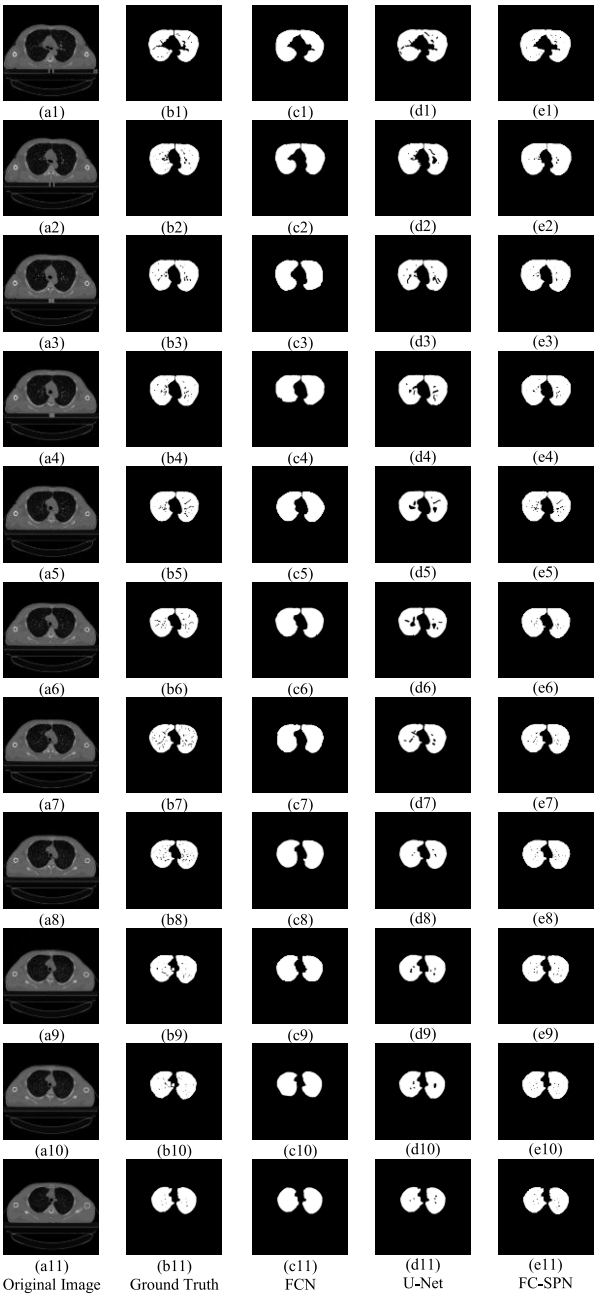

FIGURE 8. Segmentation results for the 11 CT lung slices extracted from C0017 in the PDDCA dataset using the FCN, U-Net and FC-SPN models. The first column shows the original images. The second column shows manual segmentation results. The third to fifth columns present the segmentation results of the FCN, U-Net and FC-SPN models, respectively.

V. DISCUSSION

A. PARAMETER SELECTION FOR THE FC-PCNN MODELS

An open problem of the PCNN models is how to optimize and select the model parameters. Most of the traditional PCNN models requires the tuning of at least 3 parameters when segmenting different images. Only the SPN model needs to tune only one parameter (γ_1) for dealing with different images. Fortunately, the proposed FC-PCNN models can simplify the parameter tuning process. Research has shown that all FC-PCNN models simply need to tune one parameter since the *CMFC* can provide more useful information. This improvement can be observed in Table 3.

From Table 3, we can see that the FC-FULL-PCNN only needs to tune parameter V_T, which is highlighted in bold and italic font, when segmenting different images. Similarly, γ_1 of the FC-SPN model and h of the FC-ICM, FC-SCM and FC-SPCNN models are the only parameters that must be tuned when dealing with different images. However, it is still difficult to select the optimal value of a single tuning parameter in practical applications. To solve this problem, we present a general tuning strategy in terms of the dynamic range of the parameters. Simply, dichotomization using the

TABLE 3. The tuned parameter values of the FC-PCNN models in Fig. 3 and Fig. 4.

Image	FC-FULL-PCNN /(αF, VF, αL, VL, αT, β,VT)	FC-SPN /(τ, V_U, V_γ, γ_1)	FC-ICM /(*f*, *g*, *h*)	FC-SCM /(*f*, *g*, *γ*, *h*)	FC-SPCNN /(*f*, *g*, *h*)
T-shape	(0.1, 0.4, 1.0,0.4,1, 0.1, ***110.0***)	(0.01,0.5,100, ***0.76***)	(0.9,0.44,***87.0***)	(0.9,0.44,1.0,***75***)	(0.9,0.44,***76***)
ThreeObj	(0.1, 0.4, 1.0,0.4,1, 0.1,***21.4***)	(0.01,0.5,100, ***0.72***)	(0.9,0.44,***60.4***)	(0.9,0.44,1.0,***49***)	(0.9,0.44,***71***)
Liver_A	(0.1, 0.4, 1.0,0.4,1, 0.1,***20.0***)	(0.01,0.5,100, ***0.66***)	(0.9,0.44,***81.0***)	(0.9,0.44,1.0,***62***)	(0.9,0.44,***62***)
Liver_B	(0.1, 0.4, 1.0,0.4,1, 0.1,***20.2***)	(0.01,0.5,100, ***0.64***)	(0.9,0.44,***82.0***)	(0.9,0.44,1.0,***64***)	(0.9,0.44,***65***)
Brain	(0.1, 0.4, 1.0,0.4,1, 0.1,***20.5***)	(0.01,0.5,100, ***0.66***)	(0.9,0.44,***83.0***)	(0.9,0.44,1.0,***66***)	(0.9,0.44,***66***)
Lung	(0.1,0.4,1.0,0.4,1.0,0.1,***20.2***)	(0.01,0.5,100, ***0.65***)	(0.9,0.44,***82.0***)	(0.9,0.44,1.0,***68.6***)	(0.9,0.44,***68.6***)
Kidney	(0.1,0.4,1.0,0.4,1.0,0.1,***21.5***)	(0.01,0.5,100, ***0.74***)	(0.9,0.44,***86.0***)	(0.9,0.44,1.0,***72***)	(0.9,0.44,***72***)

median value is adopted to test the value of the parameters with dynamic ranges of [0,1] or [0, 255]. In this way, the optimal value will be found quickly. In addition, experiential values can also be used to support the parameter selection process. Medical images collected from the same imaging modality have similar distributions of gray levels and noise patterns; hence, the parameters can be set to similar values. Determining the optimal values based on prior knowledge or the suggested values in the literature is a convenient method.

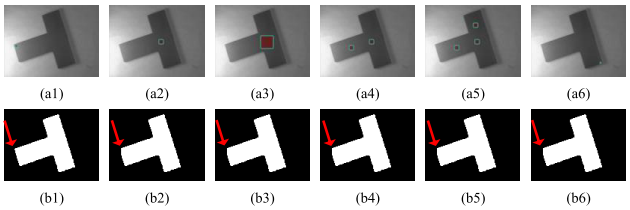

FIGURE 9. Segmentation results of the T-shape image using the FC-SPN model with different seed points. The first row shows six cases with different sizes, locations and numbers of seed points. The second row shows the segmentation results. The red arrow marks the subtle differences in the segmentation results.

B. SEED POINT SELECTION FOR FC

Seed point selection is a key step in FC, and it directly affects the performance of the proposed FC-SPN models. Here, two aspects of seed point selection are discussed. First, the influence of seed point placement is analyzed based on the experiment. Fig. 9 demonstrates the segmentation results of the T-shape image using the FC-SPN model with different seed points. The seed points are highlighted with a red rectangle surrounded by green lines. Different sizes, locations, and numbers of seed points have similar segmentation results (the second column to the fifth column). This finding means that the influence of seed point selection on the final segmentation results is very limited.

Second, attention is paid to the general seed point selection strategy. The study found that seed point selection is heavily dependent on the number and connectivity of the target to be divided. If the image has only one target (for instance, the T-shaped object in the T-shape image), one seed point in the target is enough to obtain acceptable segmentation results. However, regarding the images with multiple targets (*e.g.*, three objects in the ThreeObj image), at least one seed point needs to be placed in each target region. Therefore, the general strategy for seed point selection is to arrange at least one seed point into each separated target region in the images. Placing more seed points has no obvious influence on the performance of the FC-PCNN models.

VI. CONCLUSIONS

A novel strategy for improving the performance of the PCNN models in medical image segmentation is proposed. Considering that digital images are fuzzy by nature, a characteristic matrix of fuzzy connectedness is introduced into the iterative procedure of the PCNN models for the first time. Then, a general solution for constructing the framework of FC-PCNN models is presented. Benefitting from the intensity information and spatial relationship provided by the *CMFC*, the FC-PCNN models show great capacity to handle difficult medical image segmentation problems; traditional PCNN models often fail when encountering these medical image segmentation tasks. Compared with classic neural network and deep learning methods, much compute time and labor costs are reduced since the proposed FC-PCNN models do not require training. In addition, the pattern of single-parameter tuning in the FC-PCNN models reveals the potential to develop an automatic parameter selection scheme, which is desirable in practical applications. This will be the topic of our next work.

ACKNOWLEDGMENT

The authors would like to thank the anonymous reviewers for their helpful comments.

REFERENCES

[1] J. K. Udupa, D. Odhner, L. Zhao, Y. Tong, M. M. S. Matsumoto, K. C. Ciesielski, A. X. Falcao, P. Vaideeswaran, V. Ciesielski, B. Saboury, S. Mohammadianrasanani, S. Sin, R. Arens, and D. A. Torigian, "Body-wide hierarchical fuzzy modeling, recognition, and delineation of anatomy in medical images," *Med. Image Anal.*, vol. 18, no. 5, pp. 752–771, Jul. 2014.

[2] K. M. Meiburger, U. R. Acharya, and F. Molinari, "Automated localization and segmentation techniques for B-mode ultrasound images: A review," *Comput. Biol. Med.*, vol. 92, pp. 210–235, Jan. 2018.
[3] P. Bai, J. K. Udupa, Y. Tong, S. Xie, and D. A. Torigian, "Body region localization in whole-body low-dose CT images of PET/CT scans using virtual landmarks," *Med. Phys.*, vol. 46, no. 3, pp. 1286–1299, Mar. 2019.
[4] S. Masood, M. Sharif, A. Masood, M. Yasmin, and M. Raza, "A survey on medical image segmentation," *Current Med. Imag. Rev.*, vol. 11, no. 1, pp. 3–14, Feb. 2015.
[5] S. Hussein, U. Bagci, A. Green, A. Watane, D. Reiter, X. Chen, G. Z. Papadakis, B. Wood, A. Cypess, and M. Osman, "Automatic segmentation and quantification of white and brown adipose tissues from PET/CT scans," *IEEE Trans. Med. Imag.*, vol. 36, no. 3, pp. 734–744, Mar. 2017.
[6] H. R. Torres, S. Queirós, P. Morais, B. Oliveira, J. C. Fonseca, and J. L. Vilaça, "Kidney segmentation in ultrasound, magnetic resonance and computed tomography images: A systematic review," *Comput. Methods Programs Biomed.*, vol. 157, pp. 49–67, Apr. 2018.
[7] S. Moccia, E. De Momi, S. El Hadji, and L. S. Mattos, "Blood vessel segmentation algorithms—Review of methods, datasets and evaluation metrics," *Comput. Methods Programs Biomed.*, vol. 158, pp. 71–91, May 2018.
[8] E. Smistad, T. L. Falch, M. Bozorgi, A. C. Elster, and F. Lindseth, "Medical image segmentation on GPUs—A comprehensive review," *Med. Image Anal.*, vol. 20, no. 1, pp. 1–18, Feb. 2015.
[9] M. Sezgin and B. Sankur, "Survey over image thresholding techniques and quantitative performance evaluation," *J. Electron. Imag.*, vol. 13, no. 1, pp. 146–168, Jan. 2004.
[10] X. Chen and L. Pan, "A survey of graph cuts/graph search based medical image segmentation," *IEEE Rev. Biomed. Eng.*, vol. 11, pp. 112–124, 2018.
[11] A. K. Jain, "Data clustering: 50 years beyond K-means," *Pattern Recognit. Lett.*, vol. 31, no. 8, pp. 651–666, Jun. 2010.
[12] Q. Liu, H. Mohy-ud-Din, N. E. Boutagy, M. Jiang, S. Ren, J. C. Stendahl, A. J. Sinusas, and C. Liu, "Fully automatic multi-atlas segmentation of CTA for partial volume correction in cardiac SPECT/CT," *Phys. Med. Biol.*, vol. 62, no. 10, pp. 3944–3957, May 2017.
[13] J. S. Duncan and N. Ayache, "Medical image analysis: Progress over two decades and the challenges ahead," *IEEE Trans. Pattern Anal. Mach. Intell.*, vol. 22, no. 1, pp. 85–106, Jan. 2000.
[14] J. Canny, "A computational approach to edge detection," *IEEE Trans. Pattern Anal. Mach. Intell.*, vol. PAMI-8, no. 6, pp. 679–698, Nov. 1986.
[15] A. X. Falcão, J. K. Udupa, S. Samarasekera, S. Sharma, B. E. Hirsch, and R. D. A. Lotufo, "User-steered image segmentation paradigms: Live wire and live lane," *Graph. Models Image Process.*, vol. 60, no. 4, pp. 233–260, Jul. 1998.
[16] X. Muñoz, J. Freixenet, X. Cufí, and J. Martí, "Strategies for image segmentation combining region and boundary information," *Pattern Recognit. Lett.*, vol. 24, nos. 1–3, pp. 375–392, Jan. 2003.
[17] M. Esfandiarkhani and A. H. Foruzan, "A generalized active shape model for segmentation of liver in low-contrast CT volumes," *Comput. Biol. Med.*, vol. 82, pp. 59–70, Mar. 2017.
[18] T. F. Cootes, G. J. Edwards, and C. J. Taylor, "Active appearance models," *IEEE Trans. Pattern Anal. Mach. Intell.*, vol. 23, no. 6, pp. 681–685, Jun. 2001.
[19] T. McInerney and D. Terzopoulos, "Deformable models in medical image analysis: A survey," *Med. Image Anal.*, vol. 1, no. 2, pp. 91–108, Jun. 1996.
[20] M. Kass, A. Witkin, and D. Terzopoulos, "Snakes: Active contour models," *Int. J. Comput. Vis.*, vol. 1, no. 4, pp. 321–331, Jan. 1988.
[21] R. Malladi, J. A. Sethian, and B. C. Vemuri, "Shape modeling with front propagation: A level set approach," *IEEE Trans. Pattern Anal. Mach. Intell.*, vol. 17, no. 2, pp. 158–175, Feb. 1995.
[22] P. R. Bai, Q. Y. Liu, L. Li, S. H. Teng, J. Li, and M. Y. Cao, "A novel region-based level set method initialized with mean shift clustering for automated medical image segmentation," *Comput. Biol. Med.*, vol. 43, no. 11, pp. 1827–1832, Nov. 2013.
[23] L. He, Z. Peng, B. Everding, X. Wang, C. Y. Han, K. L. Weiss, and W. G. Wee, "A comparative study of deformable contour methods on medical image segmentation," *Image Vis. Comput.*, vol. 26, no. 2, pp. 141–163, Feb. 2008.
[24] L. O. Hall, A. M. Bensaid, L. P. Clarke, R. P. Velthuizen, M. S. Silbiger, and J. C. Bezdek, "A comparison of neural network and fuzzy clustering techniques in segmenting magnetic resonance images of the brain," *IEEE Trans. Neural Netw.*, vol. 3, no. 5, pp. 672–682, Sep. 1992.
[25] T. Song, M. M. Jamshidi, R. R. Lee, and M. Huang, "A modified probabilistic neural network for partial volume segmentation in brain MR image," *IEEE Trans. Neural Netw.*, vol. 18, no. 5, pp. 1424–1432, Sep. 2007.
[26] T. Messay, R. C. Hardie, and T. R. Tuinstra, "Segmentation of pulmonary nodules in computed tomography using a regression neural network approach and its application to the lung image database consortium and image database resource initiative dataset," *Med. Image Anal.*, vol. 22, no. 1, pp. 48–62, May 2015.
[27] R. Roy, T. Chakraborti, and A. S. Chowdhury, "A deep learning-shape driven level set synergism for pulmonary nodule segmentation," *Pattern Recognit. Lett.*, vol. 123, pp. 31–38, May 2019.
[28] R. Olaf, P. Fischer, and T. Brox, "U-net: Convolutional networks for biomedical image segmentation," in *Proc. Int. Conf. Med. Image Comput. Comput.-Assist. Intervent. (MICCAI)*, Munich, Germany, Oct. 2015, pp. 234–241. [Online]. Available: https://arxiv.org/abs/1505.04597
[29] X.-Y. Zhou and G.-Z. Yang, "Normalization in training U-net for 2-D biomedical semantic segmentation," *IEEE Robot. Autom. Lett.*, vol. 4, no. 2, pp. 1792–1799, Apr. 2019.
[30] X. Ma, L. M. Hadjiiski, J. Wei, H. Chan, K. H. Cha, R. H. Cohan, E. M. Caoili, R. Samala, C. Zhou, and Y. Lu, "U-net based deep learning bladder segmentation in CT urography," *Med. Phys.*, vol. 46, no. 4, pp. 1752–1765, Apr. 2019.
[31] X. Dong, Y. Lei, T. Wang, M. Thomas, L. Tang, W. J. Curran, T. Liu, and X. Yang, "Automatic multi-organ segmentation in thorax CT images using U-net-GAN," *Med. Phys.*, vol. 46, no. 5, pp. 2157–2168, May 2019.
[32] Z. Wang, Y. Ma, F. Cheng, and L. Yang, "Review of pulse-coupled neural networks," *Image Vis. Comput.*, vol. 28, no. 1, pp. 5–13, Jan. 2010.
[33] Z. Yang, J. Lian, Y. Guo, S. Li, D. Wang, W. Sun, and Y. Ma, "An overview of PCNN model's development and its application in image processing," *Arch. Comput. Methods Eng.*, vol. 26, no. 2, pp. 491–505, Apr. 2019.
[34] M. Murugavel and J. M. Sullivan, Jr., "Automatic cropping of MRI rat brain volumes using pulse coupled neural networks," *NeuroImage*, vol. 45, no. 3, pp. 845–854, Apr. 2009.
[35] R. Eckhorn, H. J. Reitboeck, M. Arndt, and P. Dicke, "Feature linking via synchronization among distributed assemblies: Simulations of results from cat visual cortex," *Neural Comput.*, vol. 2, no. 3, pp. 293–307, Sep. 1990.
[36] K. Zhan, J. Shi, H. Wang, Y. Xie, and Q. Li, "Computational mechanisms of pulse-coupled neural networks: A comprehensive review," *Arch. Comput. Methods Eng.*, vol. 24, pp. 573–588, Jul. 2017.
[37] J. Lian, B. Shi, M. Li, Z. Nan, and Y. Ma, "An automatic segmentation method of a parameter-adaptive PCNN for medical images," *Int. J. Comput. Assist. Radiol. Surg.*, vol. 12, no. 9, pp. 1511–1519, Sep. 2017.
[38] J. M. Kinser, "A Simplified pulse-coupled neural network," *Proc. SPIE, Aerosp./Defense Sens. Controls, Int. Soc. Opt. Photon.*, vol. 56, pp. 563–567, Mar. 1996.
[39] U. Ekblad, J. M. Kinser, J. Atmer, and N. Zetterlund, "The intersecting cortical model in image processing," *Nucl. Instrum. Methods Phys. Res. A, Accel. Spectrom. Detect. Assoc. Equip.*, vol. 525, nos. 1–2, pp. 392–396, Jun. 2004.
[40] K. Zhan, H. Zhang, and Y. Ma, "New spiking cortical model for invariant texture retrieval and image processing," *IEEE Trans. Neural Netw.*, vol. 20, no. 12, pp. 1980–1986, Dec. 2009.
[41] X.-D. Gu, S.-D. Guo, and D.-H. Yu, "A new approach for automated image segmentation based on unit-linking PCNN," in *Proc. 1st Int. Conf. Mach. Learn. Cybern. (ICMLC)*, Beijing, China, Nov. 2002, pp. 175–178. [Online]. Available: https://ieeexplore.ieee.org/document/1176733?arnumber=1176733
[42] Y. Chen, S.-K. Park, Y. Ma, and R. Ala, "A new automatic parameter setting method of a simplified PCNN for image segmentation," *IEEE Trans. Neural Netw.*, vol. 22, no. 6, pp. 880–892, Jun. 2011.
[43] I. S. Hage and R. F. Hamade, "Segmentation of histology slides of cortical bone using pulse coupled neural networks optimized by particle-swarm optimization," *Comput. Med. Imag. Graph.*, vol. 37, nos. 7–8, pp. 466–474, Oct./Dec. 2013.
[44] C. Gao, D. Zhou, and Y. Guo, "Automatic iterative algorithm for image segmentation using a modified pulse-coupled neural network," *Neurocomputing*, vol. 119, pp. 332–338, Nov. 2013.
[45] J. K. Udupa and S. Samarasekera, "Fuzzy connectedness and object definition: Theory, algorithms, and applications in image segmentation," *Graph. Models Image Process.*, vol. 58, no. 3, pp. 246–261, May 1996.
[46] J. K. Udupa and P. K. Saha, "Fuzzy connectedness and image segmentation," *Proc. IEEE*, vol. 91, no. 10, pp. 1649–1669, Oct. 2003.

[47] P. Ren, M. Xu, Y. Yu, F. Chen, X. Jiang, and E. Yang, "Energy minimization with one dot fuzzy initialization for marine oil spill segmentation," *IEEE J. Ocean. Eng.*, vol. 44, no. 4, pp. 1102–1115, Jul. 2018.
[48] F. Robert, P. Simon, W. Ashley, and W. Erik. (2003). *Hypermedia Image Processing Reference*. Accessed: Feb. 12, 2020. [Online]. Available: http://homepages.inf.ed.ac.uk/rbf/HIPR2/adpthrsh.htm
[49] D. Comaniciu and P. Meer, "Mean shift: A robust approach toward feature space analysis," *IEEE Trans. Pattern Anal. Mach. Intell.*, vol. 24, no. 5, pp. 603–619, May 2002.
[50] P. Krähenbühl and V. Koltun, "Efficient inference in fully connected CRFs with Gaussian edge," in *Proc. Adv. Neural Inf. Process. Syst. (NIPS)*. Granada, Spain: Granada Congress and Exhibition Centre, Dec. 2011, pp. 109–117. [Online]. Available: https://nips.cc/Conferences/2011
[51] A. Krizhevsky, I. Sutskever, and G. Hinton, "ImageNet classification with deep convolutional neural networks," in *Proc. Adv. Neural Inf. Process. Syst. (NIPS)*. Stateline, NV, USA: Harrahs and Harveys, Dec. 2012, pp. 1097–1105. [Online]. Available: https://nips.cc/Conferences/2012
[52] J. Long, E. Shelhamer, and T. Darrell, "Fully convolutional networks for semantic segmentation," *IEEE Trans. Pattern Anal. Mach. Intell.*, vol. 39, no. 4, pp. 640–651, Apr. 2015.

PEIRUI BAI (Member, IEEE) received the B.S. degree in electrical engineering from the Taiyuan University of Science and Technology, Taiyuan, China, in 1993, the M.S. degree in circuit and system from the Taiyuan University of Technology, Taiyuan, in 2002, and the Ph.D. degree in biomedical engineering from Xi'an Jiaotong University, Xi'an, China, in 2006.

From 2010 to 2011, he was a Visiting Scholar with the Department of Biomedical Engineering, Tsinghua University School of Medicine, Beijing, China. From 2015 to 2016, he was a Visiting Scholar with the MIPG, University of Pennsylvania. His research interests include medical imaging technology, medical image analysis, visual tracking, pattern recognition, and computer vision.

Dr. Bai is a member of the China Society of Image and Graphics (CSIG) and the Chinese Society of Biomedical Engineering (CSBME).

KAI YANG received the B.S. degree in electronic information engineering from the Shandong University of Science and Technology, Qingdao, Shandong, China, in 2018, where he is currently pursuing the M.S. degree in circuit and system.

His current research interest includes pulse coupled neural networks, mainly for medical image segmentation.

XIAOLIN MIN received the B.S. degree in biomedical engineering from the Shandong University of Science and Technology, Shandong, China, in 2010, and the Ph.D. degree from the School of Precision Instrument and Opto-Electronics Engineering, Tianjin University, Tianjin, China, in 2016.

She is engaged in the research of biomedical engineering.

ZIYANG GUO received the B.S. degree in electronic information engineering from the Shandong University of Science and Technology, Qingdao, Shandong, China, in 2017, where she is currently pursuing the M.S. degree in circuit and system.

Her research interests include dorsal hand vein recognition, focus on accurate segmentation and feature extraction of vein patterns.

CHANG LI was born in Taian, Shandong, China, in 1994. He received the B.S. degree in electronic information engineering from the Shandong University of Science and Technology, Qingdao, Shandong.

Since 2017, he has been researching medical image segmentation, focusing on level set method and deep-learning algorithms.

YINGXIA FU received the B.S. degree in electrical engineering from the Taiyuan University of Technology, Taiyuan, China, in 1992.

Her research interests include image processing and analysis, visual tracking, pattern recognition, and computer vision.

CHAO HAN received the bachelor's degree in electronic information science and technology and the master's degree in signal and information processing from the North University of China, in 2005 and 2008, respectively.

From 2008 to 2019, he worked with the China Research Institute of Radio Propagation (CRIRP). Since 2019, he has been working with the Shandong University of Science and Technology. His main research interests include image processing, satellite navigation, electromagnetic environment monitoring, and so on. He is on the editorial board of the trade journal *GNSS World of China*.

XIANG LU received the B.S. degree in electronic information engineering and M.S. degree in control engineering from the Shandong University of Science and Technology, Qingdao, Shandong, China, in 2004 and 2008, respectively, where he is currently pursuing the Ph.D. degree in control science and engineering.

From 2015 to 2016, he was a Visiting Scholar with the College of Instrumentation and Electrical Engineering, Jilin University, China. His research interests include image processing and analysis, visual tracking, pattern recognition, and computer vision.

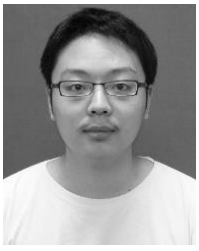

QINGYI LIU (Member, IEEE) received the M.S. degree in signal and information processing from the Shandong University of Science and Technology, Qingdao, China, in 2013, and the Ph.D. degree in signal and information processing from Shandong University, Qingdao, in 2019.

From 2015 to 2017, he was a Visiting Student with the Department of Radiology and Biomedical Imaging, Yale University, New Haven, CT, USA. His research interests include medical image, medical image processing, pattern recognition, and computer vision.